



THE UNIVERSITY *of* EDINBURGH

Edinburgh Research Explorer

Constraining human contributions to observed warming since the pre-industrial period

Citation for published version:

Gillett, NP, Kirchmeier-young, M, Ribes, A, Shiogama, H, Hegerl, GC, Knutti, R, Gastineau, G, John, JG, Li, L, Nazarenko, L, Rosenbloom, N, Seland, Ø, Wu, T, Yukimoto, S & Ziehn, T 2021, 'Constraining human contributions to observed warming since the pre-industrial period', *Nature Climate Change*.
<https://doi.org/10.1038/s41558-020-00965-9>

Digital Object Identifier (DOI):

[10.1038/s41558-020-00965-9](https://doi.org/10.1038/s41558-020-00965-9)

Link:

[Link to publication record in Edinburgh Research Explorer](#)

Document Version:

Peer reviewed version

Published In:

Nature Climate Change

General rights

Copyright for the publications made accessible via the Edinburgh Research Explorer is retained by the author(s) and / or other copyright owners and it is a condition of accessing these publications that users recognise and abide by the legal requirements associated with these rights.

Take down policy

The University of Edinburgh has made every reasonable effort to ensure that Edinburgh Research Explorer content complies with UK legislation. If you believe that the public display of this file breaches copyright please contact openaccess@ed.ac.uk providing details, and we will remove access to the work immediately and investigate your claim.



1 **Constraining human contributions to observed warming since preindustrial**

2 Nathan P. Gillett¹, Megan Kirchmeier-Young², Aurélien Ribes³, Hideo Shiogama⁴, Gabi Hegerl⁵,
3 Reto Knutti⁶, Guillaume Gastineau⁷, Jasmin G. John⁸, Lijuan Li⁹, Larissa Nazarenko¹⁰, Nan
4 Rosenbloom¹¹, Øyvind Seland¹², Tongwen Wu¹³, Seiji Yukimoto¹⁴, Tilo Ziehn¹⁵

5
6 ¹Canadian Centre for Climate Modelling and Analysis, Environment and Climate Change
7 Canada, Victoria, BC, Canada.

8 ²Climate Research Division, Environment and Climate Change Canada, Toronto, ON, Canada.

9 ³CNRM, Université de Toulouse, Météo-France, CNRS, Toulouse, France.

10 ⁴Center for Global Environmental Research, National Institute for Environmental Studies, Tsukuba,
11 Japan.

12 ⁵University of Edinburgh, School of Geosciences, Edinburgh, United Kingdom.

13 ⁶ETH Zurich, Institute for Atmospheric and Climate Science, Zurich, Switzerland.

14 ⁷LOCEAN/Institut Pierre Simon Laplace, Paris, France.

15 ⁸NOAA/OAR/Geophysical Fluid Dynamics Laboratory, Princeton, NJ, USA.

16 ⁹LASG, Institute of Atmospheric Physics, Beijing, China.

17 ¹⁰NASA Goddard Institute for Space Studies, New York, NY, USA.

18 ¹¹NCAR, Boulder, CO, USA.

19 ¹²Norwegian Meteorological Institute, Oslo, Norway.

20 ¹³Beijing Climate Center, China Meteorological Administration, Beijing, China.

21 ¹⁴Meteorological Research Institute, Tsukuba, Japan.

22 ¹⁵CSIRO Oceans and Atmosphere, Aspendale, Victoria, Australia.

23
24 **Parties to the Paris Agreement agreed to holding global average temperature increases**
25 **'well below 2 °C above pre-industrial levels' and 'pursuing efforts to limit the temperature**
26 **increase to 1.5 °C above pre-industrial levels'. Monitoring the contributions of human-**
27 **induced climate forcings to warming to date is key to understanding progress towards**
28 **these goals. Here we use climate model simulations from the Detection and Attribution**
29 **Model Intercomparison Project (DAMIP), as well as regularised optimal fingerprinting**
30 **(ROF), to estimate that anthropogenic forcings caused 0.9–1.3 °C of warming in global**
31 **mean near-surface air temperature in 2010–2019 relative to 1850–1900, compared to an**
32 **observed warming of 1.1 °C, with greenhouse gases and aerosols contributing changes of**
33 **1.2 – 1.9 °C and -0.7 – -0.1 °C, respectively, and natural forcings contributing negligibly.**
34 **These results demonstrate the substantial human influence on climate to date and the**
35 **urgency of action needed to meet the Paris Agreement goals.**

36
37 For more than twenty years, detection and attribution techniques have been used to identify
38 human influence in global temperature changes, and to quantify the contributions of individual
39 forcings to observed changes^{1–3}. The commitment of parties to the Paris Agreement⁴ to ‘holding
40 the increase in the global average temperature to well below 2 °C above pre-industrial levels, and

41 pursuing efforts to limit the temperature increase to 1.5 °C above pre-industrial levels’, and the
42 Global Stocktake process which aims to monitor progress towards the Paris goals, give new
43 relevance to efforts to quantify human climate influence to date. While the Paris Agreement is
44 not explicit about the meaning of either ‘global average temperature’ or ‘pre-industrial levels’,
45 much of the climate impacts literature on which assessment of dangerous anthropogenic
46 interference in climate is based has used globally-complete global mean near-surface air
47 temperature (GSAT) from climate models to assess future climate impacts. Therefore we
48 primarily assess human influence on GSAT here. Recent literature demonstrates that in climate
49 models this metric of global mean temperature warms more than blended sea surface
50 temperatures over ocean and near-surface air temperature over land, masked with observational
51 coverage (GMST)⁵⁻⁷. Previous attribution studies typically estimated attributable trends over the
52 past 50–60 years in GMST⁸, but estimates of warming relative to pre-industrial levels are more
53 relevant to monitoring progress towards Paris Agreement goals. While multiple possible periods
54 over the Holocene could be chosen as pre-industrial base periods⁹, we follow the IPCC Special
55 Report on 1.5 °C¹⁰ (SR1.5) and choose 1850–1900.

56

57 Comparison of global mean temperature metrics

58 Annual mean global mean temperature anomalies in the HadCRUT4¹¹ dataset, relative to 1850–
59 1900, based on an area-weighted global mean of monthly-mean anomalies are shown in Figure
60 1a. These are compared with global mean blended sea surface temperature over ocean and near
61 surface air temperature over land and ice masked with HadCRUT4 coverage⁵ (GMST, see
62 Methods) in individual CMIP6¹² historical simulations merged with SSP2-4.5¹³ simulations
63 (historical-ssp245 simulations hereafter). The simulated warming in 2010–2019 is 17% (5–95%
64 range of 10%–24%) stronger in globally-complete GSAT than in HadCRUT4-masked GMST
65 (Figure 1a), similar to previous results based on CMIP5^{14,15}, demonstrating the importance of the
66 choice of metric for assessing attributable warming. Comparing globally-complete versions of
67 GSAT and GMST, the simulated warming in GSAT is only 6% stronger (5–95% range of 2%–
68 8%). Hence the largest contribution to the enhanced warming in globally-complete GSAT versus
69 HadCRUT4-masked GMST warming comes from the observational masking.

70

71 Multiplying the observed 2010–2019 warming in HadCRUT4 GMST of 0.94 °C (5–95% range
72 of 0.90–0.99 °C, see Supplementary Table 1), by the ratio of simulated warming in globally-
73 complete GSAT to HadCRUT4-masked GMST (1.17), we infer a best estimate of observed
74 2010–2019 warming in GSAT of 1.10 °C (5–95% range of 1.01–1.20 °C). Similar calculations
75 using GISTEMP¹⁶ and NOAA GlobalTemp¹⁷ yield estimates of observed GSAT warming in
76 2010–2019 of 1.18 °C and 1.12 °C respectively (Supplementary Table 1). For the remainder of
77 the study we primarily report results based on the non-infilled HadCRUT4 dataset, and to ensure
78 a like-for-like comparison, we use masked and blended model output when comparing with

79 HadCRUT4 observations, including in all regressions. However, we report attributable warming
80 based on simulated globally-complete GSAT.

81

82 Attribution of global mean temperature changes

83 In order to quantify the contributions of individual forcings to observed trends we used the
84 CMIP6¹² DAMIP¹⁸ simulations from the thirteen CMIP6 models for which the necessary
85 simulations were available (Figure 1b, Extended Data Figure 1, Supplementary Table 2):
86 ACCESS-ESM1-5¹⁹, BCC-CSM2-MR²⁰, CanESM5²¹, CESM2²², CNRM-CM6-1²³, FGOALS-
87 g3²⁴, GFDL-ESM4²⁵, GISS-E2-1-G²⁶, HadGEM3-GC31-LL²⁷, IPSL-CM6A-LR²⁸, MIROC6²⁹,
88 MRI-ESM2-0³⁰ and NorESM2-LM³¹. We primarily used output from four experiments:
89 historical-ssp245 (driven with changes in all anthropogenic and natural forcings), hist-aer (driven
90 with changes in anthropogenic aerosol emissions and burdens only), hist-nat (driven with
91 changes in natural forcings only), and hist-GHG (driven with changes in well-mixed greenhouse
92 gas concentrations only). The CMIP6 historical-ssp245 simulations show very little net
93 anthropogenic warming prior to the 1960s (Figure 1b). This is in contrast to the CMIP5 historical
94 simulations, which showed on average approximately 0.2 °C warming by the mid-20th century⁸.
95 This could be due in part to a stronger aerosol forcing or response in these CMIP6 models. If
96 these CMIP6 simulations are correct, this would imply that there was very little net
97 anthropogenic contribution to the early 20th century warming, and that almost all anthropogenic
98 warming has occurred since the 1960s. We use global mean temperature in our main attribution
99 analysis, since previous work^{7,32} has shown that including more spatial detail may not result in
100 more robust results, perhaps because model uncertainty in spatial patterns of response is larger.
101 We use five-year means rather than decadal means^{32,33}, in an attempt to better constrain the
102 natural forcing response, which includes the short timescale response to volcanic eruptions.
103 Internal variability was estimated from intra-ensemble anomalies (see Methods).

104

105 Regression coefficients of observed temperature changes against individual models' simulated
106 response to natural and anthropogenic forcings are shown in Figure 2a (see Methods). The
107 anthropogenic response is detected using twelve of thirteen models (the uncertainty ranges on the
108 ANT regression coefficients are above zero). The only exception is ACCESS-ESM1-5, which
109 exhibits apparently unrealistic GMST evolution in its historical simulations, with almost no
110 warming prior to 1980¹⁹ (Figure 1a). By contrast, the natural forcing response is only detected
111 using CanESM5, CESM2, CNRM-CM6-1, FGOALS-g3 and IPSL-CM6A-LR, and its regression
112 coefficient is significantly less than unity using eight of the thirteen models, meaning that the
113 simulated NAT response in these models is significantly stronger than observed. The natural
114 forcing response appears to be somewhat less detectable and consistent based on these CMIP6
115 simulations than using CMIP5 simulations^{8,32-34}. Based on this regression the combined
116 anthropogenic response is of realistic magnitude in ACCESS-ESM1-5, BCC-CSM2-MR,
117 CESM2, CNRM-CM6-1, FGOALS-g3, GISS-E2-1-G, HadGEM3-GC31-LL, IPSL-CM6A-LR

118 and NorESM2-LM, significantly overestimated by CanESM5²¹, which is also apparent from
119 Figure 1a, and significantly underestimated by GFDL-ESM4, MIROC6 and MRI-ESM2-0. Note
120 that it is to be expected that significant differences between the simulated climate response in
121 models and observations can increasingly be identified as the observational record lengthens.
122

123 The realism of the scaled simulated responses to each set of forcings can be assessed by
124 comparing residual observed variability, after subtraction of these responses, with simulated
125 internal variability. The results of a residual consistency test^{32,35} (Figure 2c) indicate that
126 residuals are inconsistent with pooled simulated internal variability for ACCESS-ESM1-5,
127 CanESM5, CESM2, GISS-E2-1-G, HadGEM3-GC31-LL and NorESM2-LM, for which the
128 residual is significantly larger than expected at the 5% level, and similar results were obtained
129 for a three-way regression (Figure 2d). This could be related to the cool temperatures through the
130 mid-20th century simulated in the historical simulations of these models, with little warming
131 apparent before 1975 (Figure 1a).
132

133 In order to quantify the separate contributions of greenhouse gases and aerosols to observed
134 changes, we show the results of a three-way regression onto the simulated responses to aerosols
135 (AER, inferred from hist-aer), natural forcings (NAT, inferred from hist-nat), and greenhouse
136 gases (GHG, inferred from historical-ssp245 minus hist-aer minus hist-nat, and including the
137 response to well-mixed greenhouse gases, ozone and land-use change) in Figure 2b. The GHG
138 response is detected using eleven of thirteen models, and the AER and NAT responses are
139 detected using six. Our results suggest that ACCESS-ESM1-5, CanESM5, CESM2 and
140 HadGEM3-GC31-LL significantly overestimate the responses to both greenhouse gases and
141 aerosols, and that FGOALS-g3 underestimates them. NorESM2-LM appears to overestimate the
142 response to aerosols, while MIROC6 and MRI-ESM2-0 underestimate the response to
143 greenhouse gases. Regression coefficients from the three-way regression are poorly constrained
144 in the case of GFDL-ESM4, which may be because its hist-aer ensemble has only a single
145 ensemble member (Supplementary Table 2). Attributable temperature changes in 2010–2019
146 from the two-way regression (Figure 2e) are generally consistent between the models, albeit with
147 differences in the width of the uncertainty ranges, while individual model attributable
148 temperature changes based on the three-way regression are in some cases inconsistent between
149 models, which may reflect the effects of model uncertainty, which is not accounted here. Results
150 obtained based on a three-way regression of the observations onto the simulated response to
151 aerosols and other anthropogenic forcings (inferred from historical-ssp245 minus hist-GHG
152 minus hist-nat, and including the response to aerosols, ozone and land-use change), natural
153 forcings (from hist-nat), and well-mixed greenhouse gases (from hist-GHG) are less well-
154 constrained and show larger differences between models (Extended Data Figure 2), which may
155 be partly because in this case the weaker aerosol response is estimated from the noisy residual,
156 rather than the stronger greenhouse-gas response³⁴.
157

158 In addition to results based on individual model response patterns, we also present results based
159 on an average of responses across models, using all available ensemble members, but giving
160 equal weight to each model^{7,33,34}. Since the ROF method does not explicitly account for model
161 uncertainty, and previous work has shown that using the multi-model mean could lead to
162 overconfident results⁷, we first evaluate the multi-model mean approach in an imperfect model
163 framework^{7,32,36}. We withhold one of the thirteen models from the multi-model average, treat one
164 of its historical-ssp245 simulations as pseudo-observations, and use the remaining twelve models
165 in a multi-model analysis to calculate the best estimate and 5–95% confidence interval on its
166 GHG, AER and NAT response in globally-complete GSAT (Figure 3, *y*-axis), which can be
167 compared with the true ensemble-mean simulated value in that model (Figure 3, *x*-axis). The
168 process is repeated for all 105 historical-ssp245 simulations. The percentages of reconstructed
169 attributable changes consistent with the true simulated changes at the 10% level were 91%, 90%
170 and 79% for GHG, AER, and NAT respectively. These percentages are close to the expected
171 90% coverage ratio, particularly for GHG and AER. These results suggest that under the
172 paradigm that these models are statistically indistinguishable from the truth³⁷, the confidence
173 intervals for aerosol and greenhouse gas attributable changes are robust.

174
175 Using a multi-model average of all thirteen models, we find a detectable response to
176 anthropogenic forcing in a two-way regression, and a detectable response to GHG and AER in a
177 three-way regression, with regression coefficients consistent with one and more closely
178 constrained than based on most, though not all, individual model analyses (Figures 2a and b).
179 However, the NAT response was not detected. We find 0.9–1.3 °C (5–95% range) of warming in
180 GSAT in 2010–2019 relative to 1850–1900 attributable to anthropogenic forcings, consistent
181 with our estimate of observed warming of 1.10 °C, with GHG, AER and NAT forcings
182 contributing changes of 1.2 – 1.9 °C, -0.7 – -0.1 °C and -0.01 – 0.06 °C respectively (Table 1).
183 We find consistent residuals (Figures 2c and d), and anthropogenic-attributable warming ranges
184 which differ by no more than 0.12 °C when using either GISTEMP or NOAA GlobalTemp in
185 place of HadCRUT4 (Extended Data Figures 3 and 4, Table 1), or when using hemispheric
186 means in place of global means (Extended Data Figure 5, Table 1). Considered together with the
187 imperfect model test, these results give us confidence that our multi-model estimates of
188 attributable changes in temperature are robust. As expected, multi-model estimates of GHG-
189 attributable warming and AER-attributable cooling are both somewhat smaller in magnitude
190 when the effects of ozone are grouped with those of aerosols rather than GHGs (Extended Data
191 Figure 2, Table 1). Our estimated 5–95% range of anthropogenic-attributable warming in GMST
192 in 2010–2019 of 0.8 – 1.1 °C (Table 1) is consistent with the assessed likely range of
193 anthropogenic warming of 0.8 – 1.2 °C in 2017 in SR1.5¹⁴. This was based in part on a study
194 which regressed HadCRUT4 GMST onto the simulated anthropogenic response from an
195 impulse-response function model and obtained a 5–95% range of anthropogenic warming in
196 2017 of 0.87–1.22 °C³⁸.

197

199 As well as informing us about the contributions of different forcings to observed climate change,
200 information from detection and attribution analyses can also tell us about the degree of realism of
201 climate models and whether they overpredict or underpredict the responses to particular forcings.
202 Such information is useful for interpreting projections from these models. Much attention has
203 recently focused on the high climate sensitivity of some CMIP6 models³⁹, and while we find that
204 some of the models considered here do overestimate the response to greenhouse gases, on
205 average the greenhouse gas response of these models matches the observations closely (the best
206 estimate of the multi-model greenhouse gas regression coefficient in Figure 2b is close to one).
207 By contrast, while the multi-model mean aerosol response is not inconsistent with the
208 observations, the best estimate is that these models overestimate the response to aerosols by
209 about 30% (the best estimate of the multi-model aerosol regression coefficient in Figure 2b is
210 0.76). Given that future climate change is expected to be dominated by greenhouse gas changes,
211 overall these results increase confidence in the ensemble mean magnitude of projected warming
212 derived from these models. At the same time, the significant differences in response between
213 some models and observations identified here, are consistent with the finding that observational
214 constraints may be used to narrow the uncertainty range of projected warming based on CMIP6
215 models^{40,41}.

216
217 Estimates of greenhouse gas and aerosol-attributable warming relative to preindustrial have not
218 been previously published, but it is notable that our estimated contributions from these forcings
219 of 1.2 – 1.9 °C and -0.7 – -0.1 °C are substantially larger for example than their assessed likely
220 contributions to 1951–2010 trends in GMST of 0.5 – 1.4 °C and -0.5 – 0.1 °C respectively in
221 AR5⁸. This is probably due to our consideration of a longer period starting in 1850 and ending in
222 2019, our use of GSAT rather than GMST, and our grouping of ozone with well-mixed
223 greenhouse gases, rather than with aerosols. Nonetheless, we suggest that our results give a fairer
224 picture of the very substantial, albeit partly compensating, influences of human-induced changes
225 in greenhouse gases and aerosols to date. While the Paris Agreement⁴ is not explicit on whether
226 the ‘increase in the global average temperature’ it describes is in GMST or GSAT, nor what the
227 appropriate definition of preindustrial is, nor whether it is referring to anthropogenic warming or
228 total warming, our analysis suggests anthropogenic warming may already be close to the 1.5 °C
229 threshold.

230

231

232

233 Methods

234 We downloaded monthly mean near-surface air temperature (tas), sea surface temperature (tos),
235 and sea ice concentration (siconc) from all the CMIP6 models for which the necessary CMIP6
236 historical¹², ScenarioMIP¹³ SSP2-4.5 and DAMIP¹⁸ hist-nat and hist-aer simulations were
237 available (Supplementary Table 2). SSP2-4.5 forcings were used in the DAMIP simulations for
238 the 2015–2020 period¹⁸, so we merged CMIP6 historical simulations with SSP2-4.5 simulations
239 for the period 2015–2019 for consistency. We used ESMValTool⁴² to preprocess the model
240 output, and used Cowtan⁵ code to calculate masked and blended temperature from the model
241 output using HadCRUT4¹¹ observational masking, and using anomalies and variable sea ice
242 concentration⁵. We calculated 5-year mean global means of these data using area-weighting, for
243 the period January 1850 to December 2019 to give a vector with 34 elements, and then
244 subtracted the long-term mean to give anomalies. Due to limited availability of the land-sea
245 mask from some models, the land-sea mask from CNRM-CM6-1, regridded onto a 5°×5° grid,
246 was used for all models.

247

248 Observed GMST was calculated from HadCRUT4¹¹ monthly anomalies by area weighting,
249 taking 5-year means, and subtracting the long-term mean to give anomalies. The median dataset
250 was used for the main analysis results, and each of the 100 members of the ensemble dataset
251 were treated in the same way and used to derive uncertainties in the multi-model attributable
252 warming estimates (see also Extended Data Figure 6). The uncertainty range in inferred observed
253 GSAT warming was obtained by randomly sampling a HadCRUT4 ensemble member, and the
254 ratio of GSAT to GMST warming from an individual historical-ssp245 simulation, taking the
255 product, and repeating 10000 times, with equal weight given to each CMIP6 model. The
256 NOAAGlobalTemp¹⁷ (v5) dataset starts in 1880, but our analysis required data from 1850, so we
257 concatenated HadCRUT4 anomalies relative to the NOAAGlobalTemp 1971–2000 base period
258 over the 1850–1879 period with NOAAGlobalTemp, and then calculated global mean 5-yr mean
259 anomalies as for HadCRUT4. The GISTEMP¹⁶ (v4) data are available on a 2°×2° grid, so we
260 first interpolated onto the HadCRUT4 5°×5° grid. We then concatenated with HadCRUT4
261 anomalies relative to the GISTEMP base period of 1951–1980 over the period 1850–1879, since
262 GISTEMP starts in 1880. We then calculated global-mean 5-yr anomalies as for the other
263 datasets. Five-year mean hemispheric means (Extended Data Figure 5) were calculated in the
264 same way from gridded anomalies in masked and blended model output and observations.

265

266 An optimal detection analysis was performed using the Regularised Optimal Fingerprinting
267 algorithm^{32,35}, implemented in Python⁴³. This technique is a variant of linear regression, in which

268 the time-series of observed GMST changes Y is regressed onto the simulated responses to sets of
269 forcings X_i , i.e.

$$Y = \sum \beta_i X_i + \epsilon,$$

270 where ϵ denotes internal variability. A total least squares algorithm was used to account for noise
271 in the regressors X_i , i.e. the fact that simulated responses to forcings are affected by internal
272 variability (due to small ensemble sizes)³⁵. Key detection and attribution diagnoses were derived
273 from the inferred scaling factors β_i . The response to forcing i is detected if β_i is significantly non-
274 zero. Attribution further requires β_i being consistent with unity (i.e., consistency between the
275 observed and simulated responses). Optimal estimation within this statistical model requires an
276 estimate of the covariance matrix of ϵ , Σ , which is estimated from a sample of internal variability
277 realisations simulated by the available climate models. Realisations of internal variability were
278 calculated from all available ensembles of size greater than one (Supplementary Table 2), by
279 subtracting the ensemble mean, and then inflating anomalies by $\sqrt{\frac{N}{N-1}}$ where N is the ensemble
280 size, to account for the subtraction of the ensemble mean. Note that some of the models included
281 here, particularly BCC-CSM2-MR, CNRM-CM6-1 and IPSL-CM6A-LR, have very high
282 internal variability⁴⁴, which will tend to inflate uncertainties compared to similar studies
283 performed using CMIP5⁸. For an ensemble of size N , $N-1$ anomaly segments were calculated,
284 since the N^{th} sample calculated in this way is a linear combination of the other $N-1$ segments.
285 This gave rise to 478 realisations of internal variability, which were used in all attribution
286 analyses shown in this study. After pooling realisations across simulation type and model, half of
287 these realisations (239 realisations, which is much more than the size of our detection vector),
288 sampled alternately, were used to estimate the covariance matrix of internal variability for
289 optimization, and the remaining half were used for the residual consistency test. All analyses
290 were performed using a multi-model mean estimate of internal variability. The main analyses
291 presented used historical-ssp245 and hist-nat simulations for the two-way regressions, and
292 historical-ssp245, hist-nat, and hist-aer simulations¹⁸ for the three way regressions. Regression
293 coefficients corresponding to natural forcings, greenhouse gases and aerosols were then
294 calculated from these regression coefficients², and are shown in Figures 2a and b.

295
296 Estimates of attributable warming in GSAT in 2010–2019 were calculated by multiplying these
297 regression coefficients by the corresponding ensemble mean globally-complete GSAT response
298 in 2010–2019 to each of the forcings concerned, with the anthropogenic response inferred by
299 subtracting hist-nat from historical-ssp245 and the GHG response inferred by subtracting hist-aer
300 and hist-nat from historical-ssp245. Since uncertainty in the attributable warming arises both
301 from uncertainties in the regression coefficients and uncertainties in the ensemble mean
302 simulated response to each forcing due to internal variability, we added uncertainty components
303 from the regression coefficient and ensemble mean simulated warming in quadrature, treating
304 positive and negative departures from the best estimate separately, to allow for skewness in the
305 distribution of the regression coefficients. This approach is valid under the assumption that the

306 uncertainties in the regression coefficients and the uncertainty in the simulated warming in
307 2010–2019 are Gaussian, uncorrelated and small compared to their respective means, though as
308 noted we do make a first order correction for non-Gaussian regression coefficient distributions
309 by treating positive and negative departures separately.

310
311 Since the ratio of warming in GSAT to HadCRUT4-masked GMST varies between models
312 (Extended Data Figure 7), in the multi-model analysis we added an uncertainty contribution
313 based on the spread in this ratio across models in place of the contribution from internal
314 variability in the ensemble mean response to each forcing in an individual model. Further in the
315 multi-model analyses based on HadCRUT4, we added an additional uncertainty component to
316 account for observational uncertainty, based on the spread in regression coefficients across the
317 100-member HadCRUT4 ensemble (Extended Data Figure 6). These contributions were added in
318 quadrature to the uncertainties arising from the uncertainty in the regression coefficients, in the
319 same way as described for individual models in the previous paragraph. Attributable warming
320 ranges calculated in this way were very similar to those calculated based only on the uncertainty
321 in the regression coefficient in the multi-model analysis and for models with large ensembles,
322 and exhibited somewhat larger ranges for most models with smaller ensemble sizes (Extended
323 Data Figure 8), and substantially larger ranges for BCC-CSM2-MR due to its small ensemble
324 sizes (Supplementary Table 2) and large internal variability⁴⁴. For the multi-model analyses,
325 response patterns for each forcing were calculated by averaging individual response patterns over
326 the thirteen models used (Supplementary Table 2). Individual response patterns were averaged
327 with equal weight given to each model, and the corresponding effective ensemble size was
328 calculated and used in the analysis. Attributable changes in GMST (Table 1) were calculated in
329 the same way as for globally-complete GSAT, but used HadCRUT4-masked GMST from the
330 models in place of globally-complete GSAT.

331
332 The imperfect model test was carried out by withholding one model at a time from the multi-
333 model analysis, and using each of its historical-ssp245 simulations in turn as pseudo-
334 observations. Masked and blended temperatures (using the HadCRUT4 observational mask)
335 from this simulation were then treated as observations, and a multi-model analysis using the
336 remaining twelve models was used to infer that model's ensemble mean 2010–2019 warming in
337 response to natural forcings, greenhouse gases and aerosols, and associated 5–95% confidence
338 ranges, using the same approach as that used to derive the multi-model results presented in
339 Figure 2. Uncertainties in the attributable warming calculation were calculated as in the main
340 analysis, and uncertainties in the ensemble mean response to each forcing (shown on the *x*-axis
341 of Figure 3), were additionally accounted for when assessing consistency.

342

343 Acknowledgements

344 We thank Daithi Stone, Nicolas Bellouin, Sun Ying and Mike Winton for helpful comments on
345 the analysis and manuscript, and Lisa Bock for assistance with ESMValTool. We acknowledge
346 the World Climate Research Programme, which, through its Working Group on Coupled
347 Modelling, coordinated and promoted CMIP6, and the modelling groups whose output we use.
348

349 Author contributions

350 NPG carried out the analysis and led writing of the manuscript. MKY developed the Python code
351 used in the attribution analysis. AR developed the algorithm used in the analysis. All coauthors
352 advised on the analysis and contributed to drafting the manuscript.
353

354 Competing interests

355 The authors declare no competing interests.
356

357 Data availability

358 All figures in this manuscript use CMIP6 data available here ([https://esgf-
359 node.llnl.gov/projects/cmip6/](https://esgf-node.llnl.gov/projects/cmip6/)). The DOIs of the CMIP6 datasets used from each model were:
360 ACCESS-ESM1-5: 10.22033/ESGF/CMIP6.2288, 10.22033/ESGF/CMIP6.14362,
361 10.22033/ESGF/CMIP6.2291; BCC-CSM2-MR: 10.22033/ESGF/CMIP6.1725,
362 10.22033/ESGF/CMIP6.1726, 10.22033/ESGF/CMIP6.1732; CanESM5:
363 10.22033/ESGF/CMIP6.1303, 10.22033/ESGF/CMIP6.1305, 10.22033/ESGF/CMIP6.1317;
364 CESM2: 10.22033/ESGF/CMIP6.2185, 10.22033/ESGF/CMIP6.2187,
365 10.22033/ESGF/CMIP6.2201; CNRM-CM6-1: 10.22033/ESGF/CMIP6.1375,
366 10.22033/ESGF/CMIP6.1376, 10.22033/ESGF/CMIP6.1384; FGOALS-g3:
367 10.22033/ESGF/CMIP6.1783, 10.22033/ESGF/CMIP6.2048, 10.22033/ESGF/CMIP6.2056;
368 GFDL-ESM4: 10.22033/ESGF/CMIP6.1407, 10.22033/ESGF/CMIP6.1408,
369 10.22033/ESGF/CMIP6.1414; GISS-E2-1-G: 10.22033/ESGF/CMIP6.1400,
370 10.22033/ESGF/CMIP6.2062, 10.22033/ESGF/CMIP6.2074; HadGEM3-GC31-LL:
371 10.22033/ESGF/CMIP6.419, 10.22033/ESGF/CMIP6.471, 10.22033/ESGF/CMIP6.10845;
372 IPSL-CM6A-LR: 10.22033/ESGF/CMIP6.1534, 10.22033/ESGF/CMIP6.13801,
373 10.22033/ESGF/CMIP6.1532; MIROC6: 10.22033/ESGF/CMIP6.881,
374 10.22033/ESGF/CMIP6.894, 10.22033/ESGF/CMIP6.898; MRI-ESM2-0:
375 10.22033/ESGF/CMIP6.621, 10.22033/ESGF/CMIP6.634, 10.22033/ESGF/CMIP6.638;
376 NorESM2-LM: 10.22033/ESGF/CMIP6.502, 10.22033/ESGF/CMIP6.580,
377 10.22033/ESGF/CMIP6.604. HadCRUT4 data (version 4.6.0.0 downloaded March 24th 2020)
378 are available here (<https://www.metoffice.gov.uk/hadobs/hadcrut4/>), GISTEMP data (version 4

379 with 1200-km smoothing, downloaded April 13th 2020) are available here
380 (<https://data.giss.nasa.gov/gistemp/>), and NOAA GlobalTemp data (version 5.0.0 downloaded
381 April 13th 2020) are available here ([https://www.ncdc.noaa.gov/noaa-merged-land-ocean-global-
382 surface-temperature-analysis-noaaglobaltemp-v5](https://www.ncdc.noaa.gov/noaa-merged-land-ocean-global-surface-temperature-analysis-noaaglobaltemp-v5)).

383 Code availability

384 The analysis code used in this study is based on ESMValTool and is available here
385 (<https://github.com/ESMValGroup/ESMValTool/tree/gillett20>).

386

387 Additional information

388 Correspondence and requests for materials should be addressed to N.P.G.

389

390 References

- 391 1. Stott, P. A. & Tett, S. F. B. Scale-dependent detection of climate change. *J. Clim.* **11**,
392 3282–3294 (1998).
- 393 2. Allen, M. R. & Tett, S. F. B. Checking for model consistency in optimal fingerprinting.
394 *Clim. Dyn.* **15**, 419–434 (1999).
- 395 3. Hegerl, G. C. *et al.* Multi-fingerprint detection and attribution analysis of greenhouse gas,
396 greenhouse gas-plus-aerosol and solar forced climate change. *Clim. Dyn.* **13**, 613–634
397 (1997).
- 398 4. *Paris Agreement*. (United Nations, 2015).
- 399 5. Cowtan, K. *et al.* Robust comparison of climate models with observations using blended
400 land air and ocean sea surface temperatures. **42**, 6526–6535 (2015).
- 401 6. Richardson, M., Cowtan, K. & Millar, R. J. Global temperature definition affects
402 achievement of long-term climate goals. *Environ. Res. Lett.* **13**, (2018).
- 403 7. Schurer, A. *et al.* Estimating the Transient Climate Response from Observed Warming. *J.*
404 *Clim.* **31**, 8645–8663 (2018).
- 405 8. Bindoff, N. L. *et al.* Detection and attribution of climate change: From global to regional. in
406 *Climate Change 2013 the Physical Science Basis: Working Group I Contribution to the*
407 *Fifth Assessment Report of the Intergovernmental Panel on Climate Change* (eds.
408 Stocker, T. F., Qin, D., Pattner, G.-K., Tignor, M. & Allen) vol. 9781107057 867–952
409 (Cambridge University Press, 2013).
- 410 9. Schurer, A. P., Mann, M. E., Hawkins, E., Tett, S. F. B. & Hegerl, G. C. Importance of the
411 pre-industrial baseline for likelihood of exceeding Paris goals. *Nat. Clim. Chang.* **7**, 563–
412 567 (2017).
- 413 10. Masson-Delmotte, V. *et al.* *Global warming of 1.5°C An IPCC Special Report. Report of*
414 *the Intergovernmental Panel on Climate Change* (2018).
- 415 11. Morice, C. P., Kennedy, J. J., Rayner, N. A. & Jones, P. D. Quantifying uncertainties in
416 global and regional temperature change using an ensemble of observational estimates:
417 The HadCRUT4 data set. *J. Geophys. Res. Atmos.* (2012) doi:10.1029/2011JD017187.
- 418 12. Eyring, V. *et al.* Overview of the Coupled Model Intercomparison Project Phase 6
419 (CMIP6) experimental design and organization. *Geosci. Model Dev.* **9**, 1937–1958
420 (2016).
- 421 13. O’Neill, B. C. *et al.* The Scenario Model Intercomparison Project (ScenarioMIP) for

- 422 CMIP6. *Geosci. Model Dev.* (2016) doi:10.5194/gmd-9-3461-2016.
- 423 14. Allen, M. R. *et al.* *IPCC: Framing and Context. Global warming of 1.5°C. An IPCC Special*
424 *Report* (2018).
- 425 15. Rogelj, J., Forster, P. M., Kriegler, E., Smith, C. J. & Séférian, R. Estimating and tracking
426 the remaining carbon budget for stringent climate targets. *Nature* **571**, 335–342 (2019).
- 427 16. Lenssen, N. J. L. *et al.* Improvements in the GISTEMP Uncertainty Model. *J. Geophys.*
428 *Res. Atmos.* **124**, 6307–6326 (2019).
- 429 17. Huang, B. *et al.* Uncertainty estimates for sea surface temperature and land surface air
430 temperature in NOAA GlobalTemp version 5. *J. Clim.* **33**, 1351–1379 (2020).
- 431 18. Gillett, N. P. *et al.* The Detection and Attribution Model Intercomparison Project
432 (DAMIP~v1.0) contribution to CMIP6. *Geosci. Model Dev.* **9**, 3685–3697 (2016).
- 433 19. Ziehn, T. *et al.* The Australian Earth System Model: ACCESS-ESM1.5. *J. South.*
434 *Hemisph. Earth Syst. Sci.* (2020) doi:10.1071/es19035.
- 435 20. Wu, T. *et al.* The Beijing Climate Center Climate System Model (BCC-CSM): The main
436 progress from CMIP5 to CMIP6. *Geosci. Model Dev.* (2019) doi:10.5194/gmd-12-1573-
437 2019.
- 438 21. Swart, N. C. *et al.* The Canadian Earth System Model version 5 (CanESM5.0.3). *Geosci.*
439 *Model Dev. Discuss.* (2019) doi:10.5194/gmd-2019-177.
- 440 22. Danabasoglu, G. *et al.* The Community Earth System Model Version 2 (CESM2). *J. Adv.*
441 *Model. Earth Syst.* (2020) doi:10.1029/2019MS001916.
- 442 23. Voldoire, A. *et al.* Evaluation of CMIP6 DECK Experiments With CNRM-CM6-1. *J. Adv.*
443 *Model. Earth Syst.* (2019) doi:10.1029/2019MS001683.
- 444 24. Li, L. J. *et al.* The Flexible Global Ocean–Atmosphere–Land System Model Grid-Point
445 Version 3 (FGOALS-g3): Description and Evaluation. *J. Adv. Model. Earth Syst.* (2020)
446 doi:10.1029/2019MS002012.
- 447 25. Dunne, J. P. *et al.* The GFDL Earth System Model version 4.1 (GFDL-ESM4.1): Overall
448 coupled model description and simulation characteristics. *J. Adv. Model. Earth Syst.*
449 (2020) doi:10.1029/2019MS002015.
- 450 26. Kelley, M. *et al.* GISS-E2.1: Configurations and Climatology. *J. Adv. Model. Earth Syst.*
451 (2020) doi:10.1029/2019MS002025.
- 452 27. Williams, K. D. *et al.* The Met Office Global Coupled Model 3.0 and 3.1 (GC3.0 and
453 GC3.1) Configurations. *J. Adv. Model. Earth Syst.* (2018) doi:10.1002/2017MS001115.
- 454 28. Boucher, O., Servonnat, J., Albright, A. L., Aumont, O. & Balkanski, Y. Presentation and
455 evaluation of the IPSL-CM6A-LR climate model. *J. Adv. Model. Earth Syst.* (2020)
456 doi:10.1029/2019MS002010.
- 457 29. Tatebe, H. *et al.* Description and basic evaluation of simulated mean state, internal
458 variability, and climate sensitivity in MIROC6. *Geosci. Model Dev.* (2019)
459 doi:10.5194/gmd-12-2727-2019.
- 460 30. Yukimoto, S. *et al.* The Meteorological Research Institute Earth system model version
461 2.0, MRI-ESM2.0: Description and basic evaluation of the physical component. *J.*
462 *Meteorol. Soc. Japan* **97**, 931–965 (2019).
- 463 31. Seland, Ø. *et al.* The Norwegian Earth System Model, NorESM2 – Evaluation of
464 the CMIP6 DECK and historical simulations. *Geosci. Model Dev. Discuss.* (2020)
465 doi:10.5194/gmd-2019-378.
- 466 32. Ribes, A. & Terray, L. Application of regularised optimal fingerprinting to attribution. Part
467 II: Application to global near-surface temperature. *Clim. Dyn.* **41**, 2837–2853 (2013).
- 468 33. Gillett, N. P., Arora, V. K., Matthews, D. & Allen, M. R. Constraining the ratio of global
469 warming to cumulative CO₂ emissions using CMIP5 simulations. *J. Clim.* **26**, 6844–6858
470 (2013).
- 471 34. Jones, G. S., Stott, P. A. & Christidis, N. Attribution of observed historical near-surface
472 temperature variations to anthropogenic and natural causes using CMIP5 simulations. *J.*

- 473 *Geophys. Res. Atmos.* **118**, 4001–4024 (2013).
- 474 35. Ribes, A., Planton, S. & Terray, L. Application of regularised optimal fingerprinting to
475 attribution. Part I: method, properties and idealised analysis. *Clim. Dyn.* **41**, 2817–2836
476 (2013).
- 477 36. Shiogama, H. *et al.* Predicting future uncertainty constraints on global warming
478 projections. *Sci. Rep.* (2016) doi:10.1038/srep18903.
- 479 37. Annan, J. D. & Hargreaves, J. C. Reliability of the CMIP3 ensemble. *Geophys. Res. Lett.*
480 (2010) doi:10.1029/2009GL041994.
- 481 38. Haustein, K. *et al.* A real-time Global Warming Index. *Sci. Rep.* (2017)
482 doi:10.1038/s41598-017-14828-5.
- 483 39. Zelinka, M. D. *et al.* Causes of Higher Climate Sensitivity in CMIP6 Models. *Geophys.*
484 *Res. Lett.* (2020) doi:10.1029/2019GL085782.
- 485 40. Tokarska, K. B. *et al.* Past warming trend constrains future warming in CMIP6 models.
486 *Sci. Adv.* (2020) doi:10.1126/sciadv.aaz9549.
- 487 41. Liang, Y., Gillett, N. P. & Monahan, A. H. Climate model projections of 21st century global
488 warming constrained using the observed warming trend. *Geophys. Res. Lett.* (2020)
489 doi:10.1029/2019GL086757.
- 490 42. Eyring, V. *et al.* ESMValTool (v1.0)-a community diagnostic and performance metrics tool
491 for routine evaluation of Earth system models in CMIP. *Geosci. Model Dev.* (2016)
492 doi:10.5194/gmd-9-1747-2016.
- 493 43. Kirchmeier-Young, M. C., Zwiers, F. W. & Gillett, N. P. Attribution of extreme events in
494 Arctic Sea ice extent. *J. Clim.* **30**, 553–571 (2017).
- 495 44. Parsons, L. A., Brennan, M. K., Wills, R. C. J. & Proistosescu, C. Magnitudes and Spatial
496 Patterns of Interdecadal Temperature Variability in CMIP6. *Geophys. Res. Lett.* (2020)
497 doi:10.1029/2019GL086588.
- 498
- 499

	Two-way regression		Three-way regression		
	ANT	NAT	GHG	AER	NAT
Main analysis	0.92 – 1.30	-0.02 – 0.05	1.16 – 1.95	-0.73 – -0.14	-0.01 – 0.06
hist-GHG			1.06 – 1.94	-0.71 – -0.03	-0.01 – 0.07
Hemispheric	0.94 – 1.29	-0.02 – 0.04	1.36 – 2.04	-0.84 – -0.29	-0.02 – 0.05
GISTEMP	1.04 – 1.42	-0.05 – 0.02	1.34 – 2.12	-0.78 – -0.19	-0.04 – 0.03
NOAA	1.02 – 1.39	-0.03 – 0.05	1.37 – 2.15	-0.85 – -0.25	-0.05 – 0.05
GMST	0.80 – 1.10	-0.02 – 0.04	1.04 – 1.69	-0.65 – -0.14	-0.01 – 0.04

501

502 **Table 1 Multi-model estimates of attributable temperature change between 1850–1900 and**
503 **2010–2019 in °C.** The table shows 5–95% confidence ranges in attributable warming from the
504 main multi-model analysis (first row), from an equivalent analysis in which the GHG signal is
505 derived from hist-GHG, and the AER signal is derived from historical-ssp245 minus hist-GHG
506 minus hist-NAT (in this case ozone and land-use change are grouped with AER instead of GHG)
507 (second row), from an analysis identical to the main analysis except using 5-yr mean Northern
508 and Southern Hemispheric mean temperature instead of GMST (third row), from analyses
509 identical to the main analysis, except using GISTEMP (fourth row), and NOAAGlobalTemp
510 (fifth row) in place of HadCRUT4, and from an analysis identical to the main analysis, except for
511 HadCRUT4-masked GMST instead of globally-complete GSAT (sixth row).

512

513 **Figure 1: Comparison of 1850–2019 global mean temperature evolution in observations**
514 **and CMIP6 simulations.** Coloured lines in the top panel show HadCRUT4-masked blended
515 GMST⁵ anomalies relative to the 1850–1900 base period in one historical-ssp245 simulation
516 from each model. The thick brown line shows the multi-model mean, using all ensemble
517 members, but with equal weights given to each model. The thick red line shows the
518 corresponding multi-model mean of globally-complete GSAT. The thick black line shows
519 HadCRUT4¹¹. The lower panel compares HadCRUT4 GMST with simulated GMST from
520 CMIP6 historical-ssp245 simulations with anthropogenic and natural forcings, natural forcing
521 simulations, well-mixed greenhouse gas only simulations, and aerosol only simulations. The
522 multi-model mean and 5–95% ensemble range are shown, both calculated with equal weight
523 given to each model.

524
525 **Figure 2: Results of a regression analysis applied to CMIP6 models.** The left column shows
526 the results of a two-way regression of observed 5-year mean GMST onto the simulated response
527 to anthropogenic (ANT) and natural (NAT) forcings from each model individually, and the right
528 column shows the results of a corresponding three-way regression of observations onto the
529 simulated response to aerosols (AER), natural forcings (NAT) and well-mixed greenhouse gases,
530 ozone and land-use change (GHG). The top row shows regression coefficients and their 5–95%
531 confidence ranges. Regression coefficients inconsistent with zero indicate a detectable response
532 to the corresponding forcing, and regression coefficients consistent with one indicate a consistent
533 magnitude of response in model and observations. The middle row shows the *p*-value resulting
534 from a residual consistency test³⁵. The bottom row shows the 2010–2019 change in global mean
535 near-surface air temperature relative to 1850–1900 attributable to each forcing (5–95%
536 confidence ranges). The horizontal black line indicates an estimate of the observed change in
537 GSAT based on HadCRUT4.

538
539 **Figure 3: Imperfect model test of multi-model attributable warming calculation.** The *x*-axis
540 shows the simulated ensemble mean 2010–2019 temperature change relative to 1850–1900 in
541 response to aerosols only (hist-aer simulations) (blue), natural forcings only (hist-nat
542 simulations) (green) and greenhouse gases, ozone and land-use change (historical-ssp245 minus
543 hist-nat and hist-aer) (grey) in each of the thirteen models used. Each historical simulation from
544 the corresponding model was in turn treated as pseudo-observations, and the remaining twelve
545 models were together used to provide estimates of response patterns to aerosols, natural, and
546 greenhouse gas forcing in an optimal regression. The estimated attributable warming is shown on
547 the *y*-axis. Crosses show best estimates, and vertical bars show 90% confidence ranges. For
548 models with more than one historical-ssp245 simulation, confidence bars are offset along the *x*-
549 axis, to make them visible.

550
551

552 **Extended Data Figure 1: Global mean surface temperature (GMST) anomalies in all**
553 **DAMIP historical simulations.** The multi-model mean and 5–95% ensemble ranges, based on
554 all available simulations with equal weight given to each model, are shown. HadCRUT4 GMST
555 is shown in black on the top graph.

556
557 **Extended Data Figure 2: Results of a regression in which observed changes are**
558 **decomposed into the response to natural forcings, well-mixed greenhouse gases, and other**
559 **anthropogenic forcings.** As Figure 2, except that the right panels show the results of a three-
560 way regression of observations onto the simulated response to natural forcings (NAT), well-
561 mixed greenhouse gases only (GHG), and other anthropogenic forcings (OTH), consisting of
562 aerosols, ozone and land-use change. In this figure ozone and land-use change are grouped with
563 aerosols, instead of with well-mixed greenhouse gases, as in Figure 2.

564
565 **Extended Data Figure 3: Regression results based on GISTEMP.** As Figure 2, except using
566 GISTEMP in place of HadCRUT4.

567
568 **Extended Data Figure 4: Regression results based on NOAAGlobalTemp.** As Figure 2,
569 except using NOAAGlobalTemp in place of HadCRUT4.

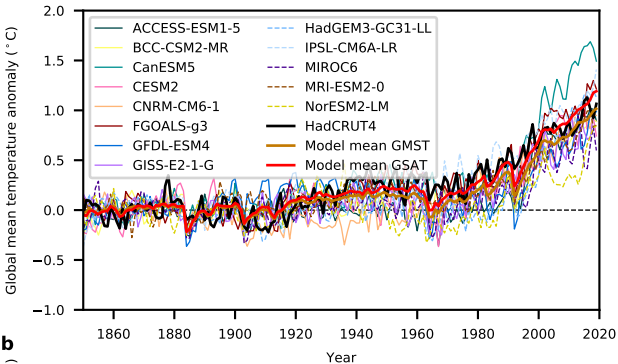
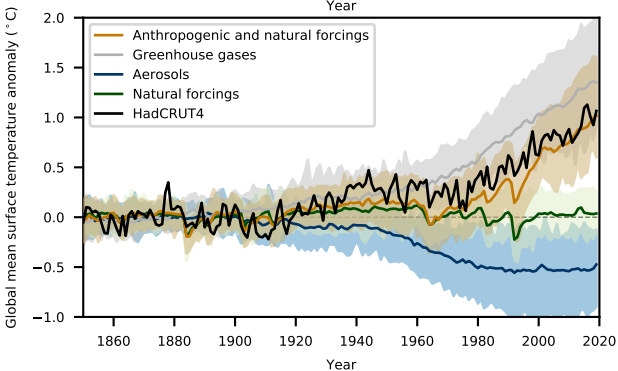
570
571 **Extended Data Figure 5: Regression results based on hemispheric means.** As Figure 2,
572 except using 5-yr mean hemispheric means in place of 5-yr mean GMST in the regressions.

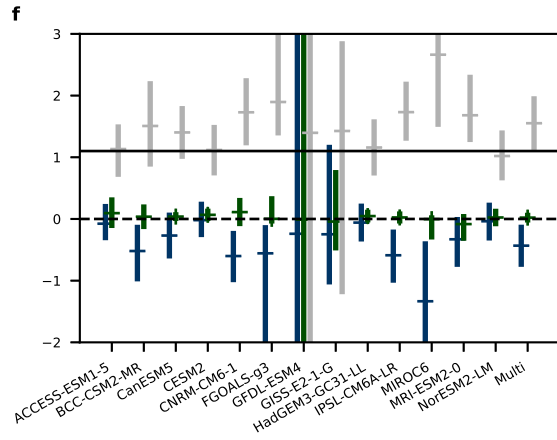
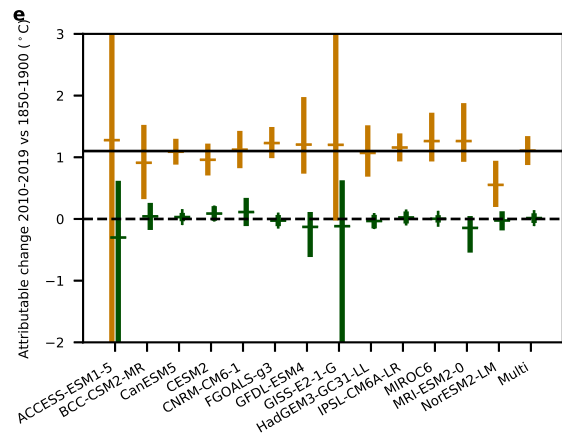
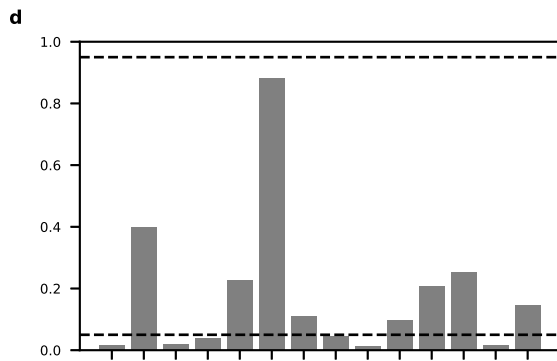
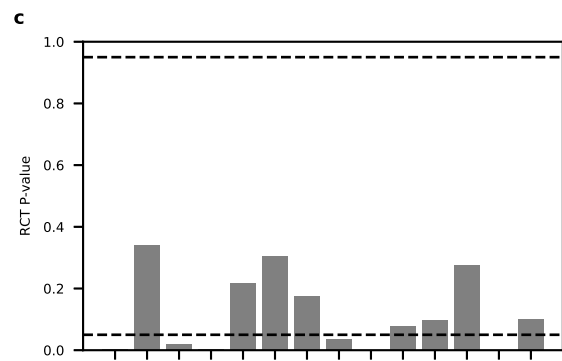
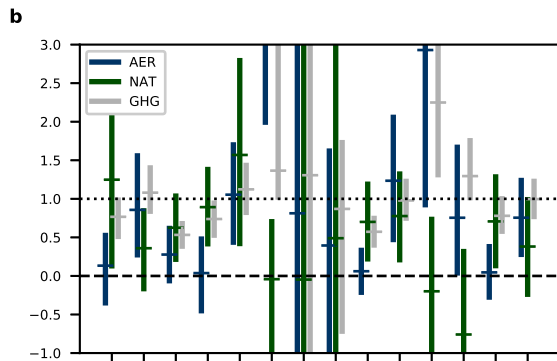
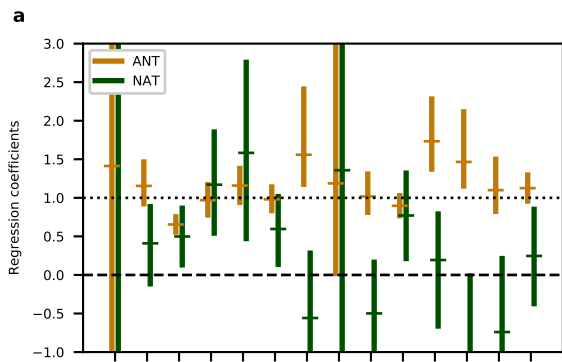
573
574 **Extended Data Figure 6: Regression coefficients derived using each of the 100 ensemble**
575 **members of HadCRUT4¹¹.** Results are shown for two-way (a) and three-way (b) multi-model
576 regression analyses, as shown in Figure 2a and b, except using each of the 100 members of the
577 HadCRUT4 ensemble dataset in turn.

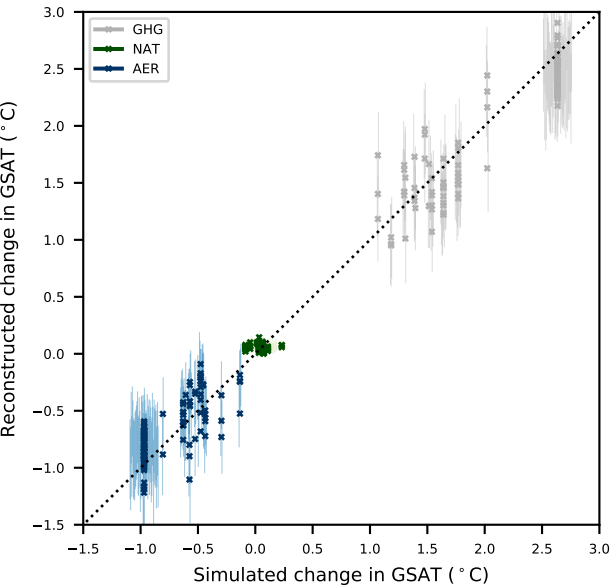
578
579 **Extended Data Figure 7: The ratio of 2010–2019 warming relative to 1850–1900 in GSAT**
580 **to HadCRUT4-masked GMST and globally-complete GMST.** The ratio of changes in GSAT
581 to HadCRUT4-masked GMST is shown in (a), and the ratio of changes in GSAT to globally-
582 complete GMST is shown in (b) for each individual historical-ssp245 simulation of each model.

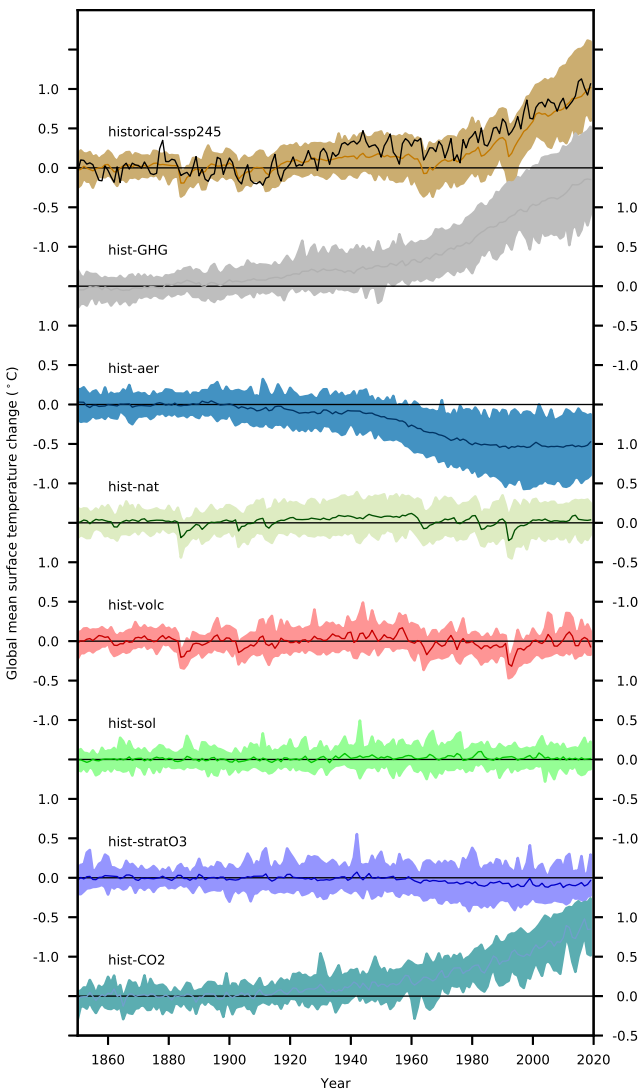
583
584 **Extended Data Figure 8: Comparison of uncertainty calculation approaches.** As Figures 2e
585 and f, except that in each case uncertainties in attributable temperature change are calculated in
586 two ways. Bars show confidence intervals calculated, as in the main analysis, accounting for
587 uncertainty in the ensemble mean simulated 2010–2019 GSAT changes in the case of the
588 individual model analyses, and accounting for uncertainties in the ratio of GSAT to GMST and
589 observational uncertainty, in the case of the multi-model analysis. Horizontal ticks show
590 confidence ranges neglecting these sources of uncertainty. The latter calculation corresponds to

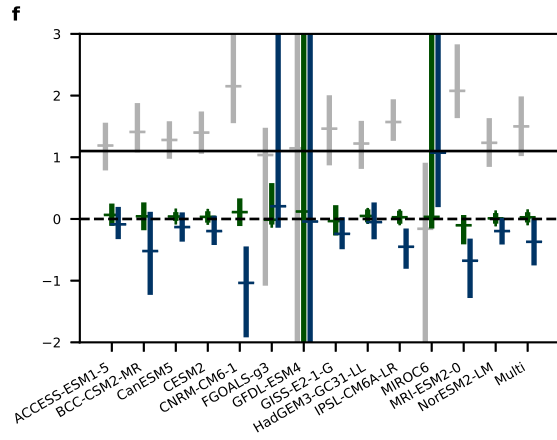
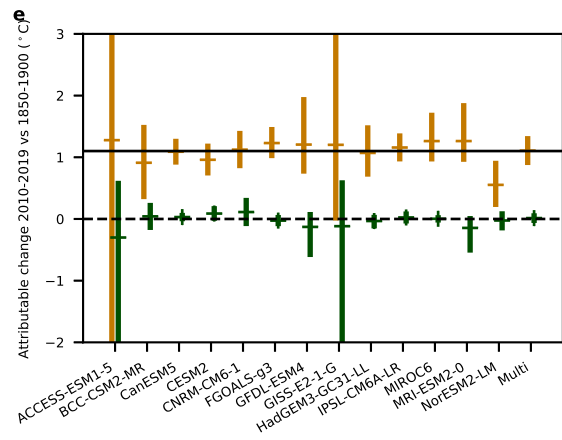
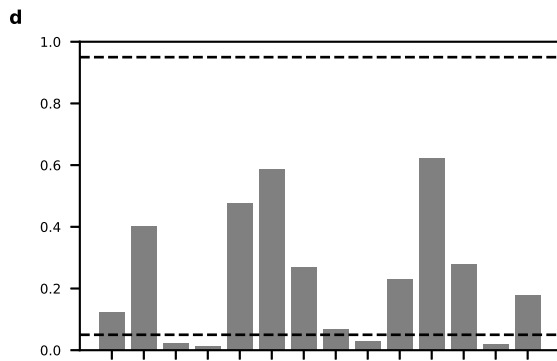
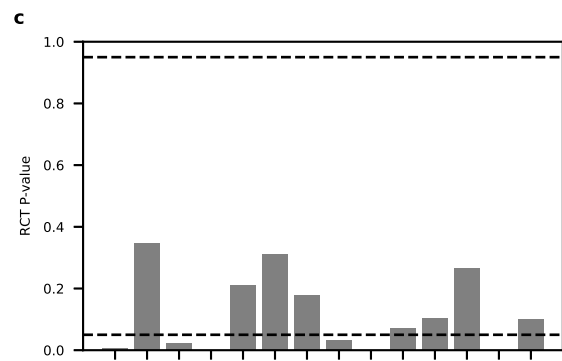
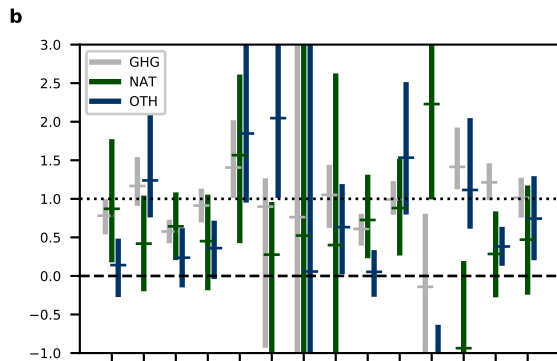
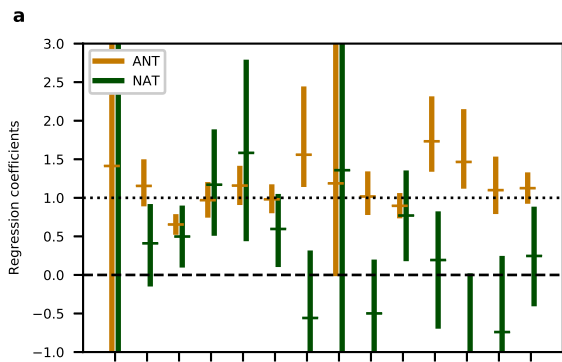
591 multiplying the 5–95% confidence range on the regression coefficient by the corresponding
592 ensemble mean simulated 2010–2019 GSAT change.

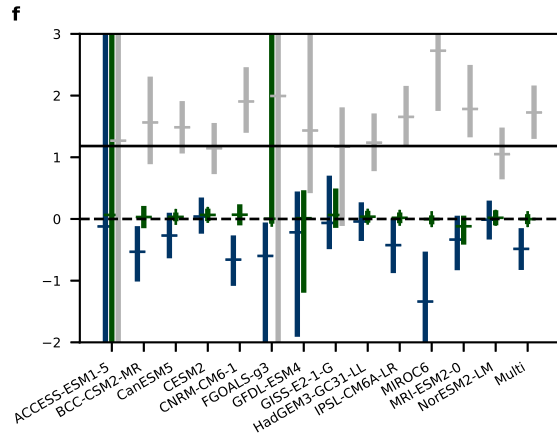
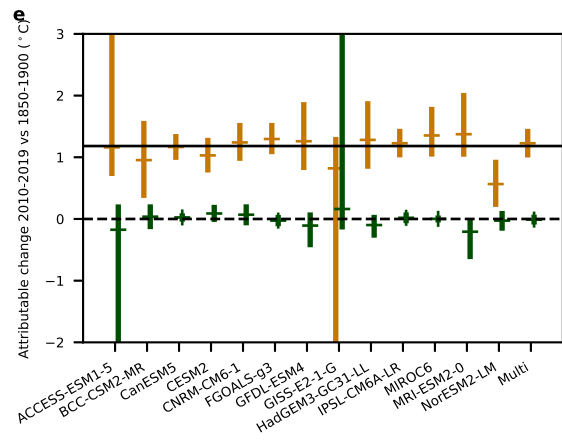
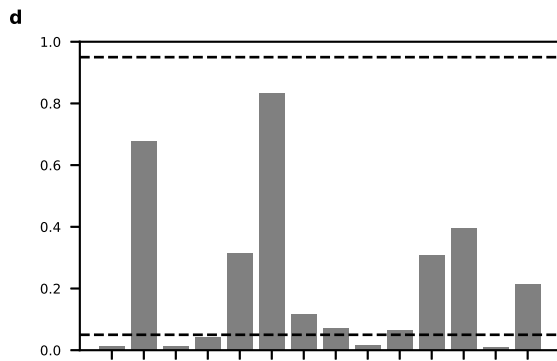
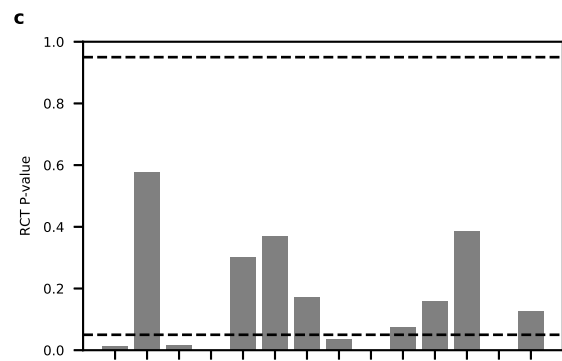
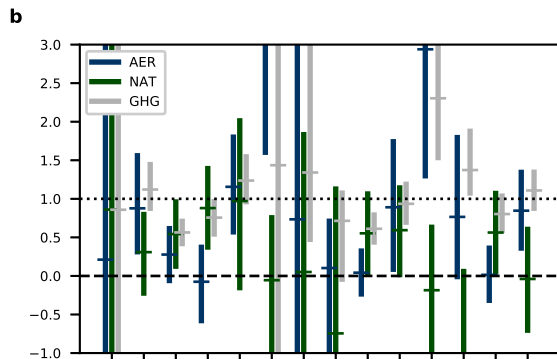
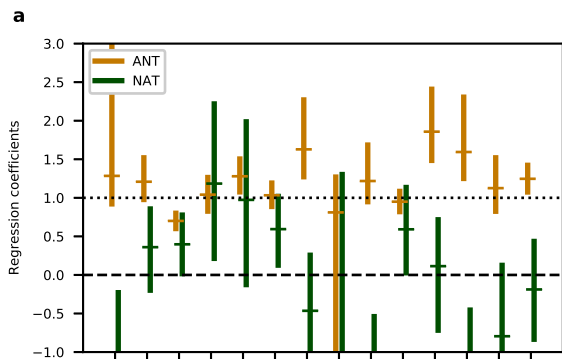
a**b**





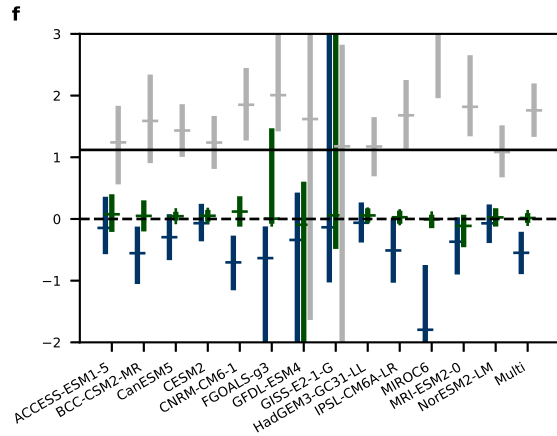
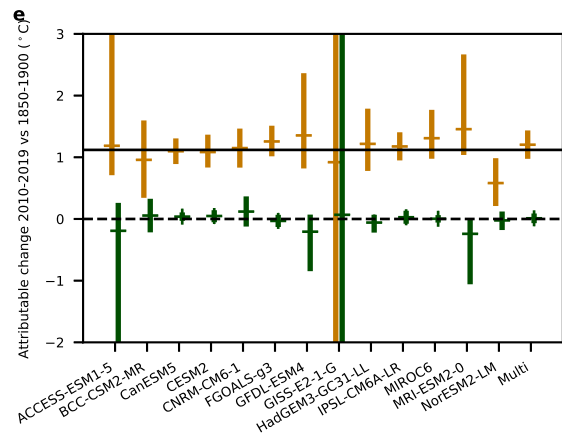
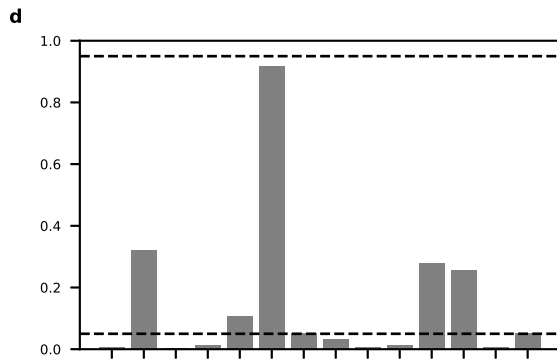
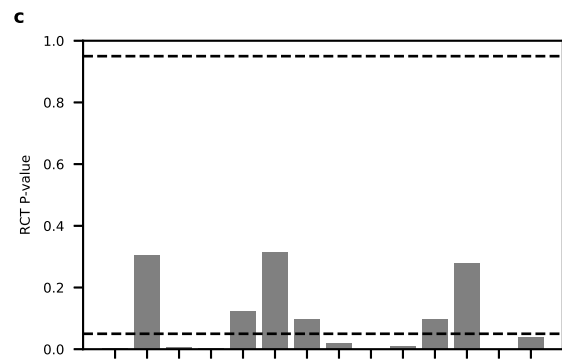
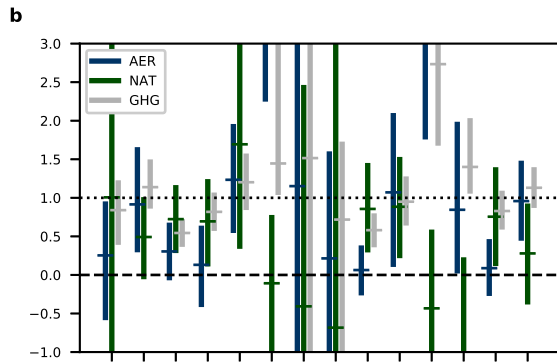
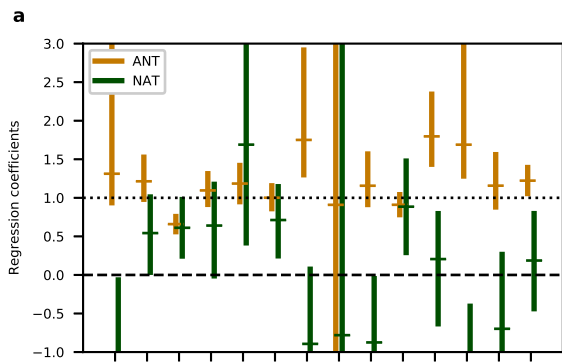






ACCESS-ESM1-5
BCC-CSM2-MR
CanESM5
CESM2
CNRM-CM6-1
FGOALS-g3
GFDL-ESM4
GISS-E2-1-G
HadGEM3-GC31-LL
IPSL-CM6A-LR
MIROC6
MRI-ESM2-0
NorESM2-LM
Multi

ACCESS-ESM1-5
BCC-CSM2-MR
CanESM5
CESM2
CNRM-CM6-1
FGOALS-g3
GFDL-ESM4
GISS-E2-1-G
HadGEM3-GC31-LL
IPSL-CM6A-LR
MIROC6
MRI-ESM2-0
NorESM2-LM
Multi



ACCESS-ESM1-5
BCC-CSM2-MR
CanESM5
CESM2
CNRM-CM6-1
FGOALS-g3
GFDL-ESM4
GISS-E2-1-G
HadGEM3-GC31-L
IPSL-CM6A-LR
MIROC6
MRI-ESM2-0
NorESM2-LM
Multi

ACCESS-ESM1-5
BCC-CSM2-MR
CanESM5
CESM2
CNRM-CM6-1
FGOALS-g3
GFDL-ESM4
GISS-E2-1-G
HadGEM3-GC31-L
IPSL-CM6A-LR
MIROC6
MRI-ESM2-0
NorESM2-LM
Multi

